Journal of Catalysis xxx (xxxx) 1–13

Contents lists available at ScienceDirect

Journal of Catalysis

journal homepage: www.elsevier.com

Synthesis of spherical, rod, or chain Ni nanoparticles and their structure–activity relationship in glucose hydrogenation reaction

Yang Fu [a], Benoit Pichon [b], François Devred [a], Michael L. Singleton [a], Sophie Hermans [a]

[a] IMCN Institute, MOST Division, UCLouvain, 1 Place Louis Pasteur, B-1348 Louvain-la-Neuve, Belgium
[b] Université de Strasbourg, CNRS, Institut de Physique et Chimie des Matériaux de Strasbourg, UMR 7504, F-67000 Strasbourg, France

ARTICLE INFO

Article history:
Received 23 June 2022
Received in revised form 5 September 2022
Accepted 26 September 2022

Keywords:
Glucose
Hydrogenation
Non-noble metals
P-dopant
Crystallinity
Amorphous

ABSTRACT

Structure-activity relationships of Ni particles with different morphologies, crystallinities and compositions were investigated for glucose hydrogenation. Nanorods and nanospheres were obtained respectively by altering hydrogen pressure during synthesis, and nanobead chains were synthesized for analogy analysis following a known procedure. Glucose hydrogenation over Ni nanosphere catalysts exhibits the lowest reaction barrier (E_a = 32 kJ/mol) compared to nanorods and nanobead chains (98 kJ/mol), and a constant sorbitol selectivity of 100 % was obtained at a temperature of 140 °C. A comprehensive characterization with ATR-IR, Raman, XPS, ICP, P-XRD, HRTEM and SAED revealed that the combined factors of poly-crystallinity, amorphous structure and P- dopant make Ni nanospheres superior. This provides a valuable path in the process of designing better non-noble catalysts to definitely avoid the use of noble metals in the future in biomass valorization reactions.

1. Introduction

Biomass is currently the only resource for the production of sustainable organic carbon and biofuels [1], and it can be used as a substitute for traditional fossil fuels to produce sustainable fuels and chemicals. The utilization of biomass can reduce the dependence on declining petroleum resources and reduce CO_2 emissions [2]. In particular, cellulose accounts for 40 % of the biomass obtained through natural photochemical processes yearly [3]. Cellulose derived products have been exploited via degradation processes by enzymes, or under critical conditions like acid or base and heterogeneous catalysis. Catalysis allows to work under softer conditions and increases selectivity. The primary product glucose is produced as a consequence of breakage of β-1,4-glycosidic bonds in cellulose [3,4]. Sorbitol is the reduction product of glucose, widely used in medical applications and in the food and cosmetic industries, which has been recognized as one of the twelve most important platform chemicals obtainable from biomass [5,6].

Sorbitol was first produced by the reduction of glucose in 1912 by Ipatieff in the presence of a nickel catalyst [7]. Since then, plenty of research has been carried out to investigate the mechanism [8–12], kinetics [13–15] and mostly the design of new catalysts for this transformation [16–18]. The applied catalyst has evolved from pure Raney-type nickel catalysts at the beginning to promoted Raney Ni, where a higher electronegativity metal or promoter is used to further enhance catalytic performance of Ni [8,19,20]. For example, since Rh has a higher electronegativity than Pt, the activation energy of glucose hydrogenation could be improved from 50 to 54 kJ/mol (Raney Ni doped with Pt) to 38–42 kJ/mol (Raney Ni doped with Rh) [21]. Later, the catalysts were further developed into supported metal nanoparticles, and the noble metals Pt, Pd, and Ru were explored as well [16,22–24]. As a result, Ru is currently the catalyst with best activity, as it is reported by Hoffer for example that 3.5–6.5 wt% of glucose in aqueous solution was 100 % converted into sorbitol with a selectivity >98 % over ~2 g of Ru/C catalyst in ~140 min.[25] Although Ru catalysts demonstrate dominant catalytic activity, considering that the industrial cost of Ru is more than 700 times higher than Ni, non-noble metal catalysts are always preferable for industry. Thus, development of low-cost catalysts has continued to be studied in parallel [17,26,27]. In addition to achieving high activity, sorbitol selectivity is also another important criterion of catalyst performance for glucose hydrogenation, since isomerization, as well as other side reactions, take place in aqueous solution under harsh conditions [28,29]. Among previously developed catalysts, Ni and Ru have the advantage of high sorbitol selectivity, by opposition to Pt, Pd metals that give lower sorbitol yields for the same glucose conversion [22,24,30]. Given the high cost of Ru mentioned above, Ni was chosen in this work to construct a more abundant and cheaper metal catalyst with a high activity and sorbitol selectivity for glucose hydrogenation.

https://doi.org/10.1016/j.jcat.2022.09.028
0021-9517/© 20XX

Unlike the supported Ni catalysts mentioned above, unsupported Ni particles are favoured in the present study to be able to investigate the structure-activities relationships induced only by the Ni particle itself. Regarding metal particles, the modification of their catalytic performance can be achieved by manipulating the morphologies including regulation of particle sizes and shapes and by tuning the composition and crystallinities [31,32]. Given that it is easier to obtain metal particles with different sizes, more research has been done on particle sizes than on shapes. Nevertheless, due to the fascination of facet effects caused by different shapes of particles, a great deal of work has been done on shaped controlled nanoparticles applied in catalytic reactions over the last two decades [33–35]. For example, Xu *et al.* have found that the rate of oxidation of styrene over silver nanocubes was more than 14 times higher than that on nanoplates and 4 times higher than that on near-spherical nanoparticles [36]. The shape of the metal nanoparticle not only has an effect on the activity, but also on product selectivity. For instance, Kim *et al.* observed a lower acetylene conversion and ethylene selectivity over spherical nanoparticles with a significant amount of (1 1 1) facets than cubic Pd nanoparticles with (1 0 0) facets for the selective hydrogenation of acetylene over Pd/Al_2O_3 catalyst [37]. Apart from the morphology of particles inducing variation of their catalytic performance, altering the crystallinity and heteroatomic doping also has raised interest since a long time. Heterogenizing metal catalysts with P has been used in electrocatalysis and thermal catalysis due to enhanced catalytic activity [38,39]. For example, P dopant in Rh catalysts can eliminate the surface hollow sites thus weakening the adsorption strength of CO, leading to a higher hydroformylation activity of Rh-P catalyst compared to Rh catalysts [39]. Ni-P/SiO_2 amorphous catalyst lost its surface active Ni atoms after it was crystallized stepwise from 673 to 873 K, leading to a higher E_a and lower TOF value for the hydrogenation of benzaldehyde [40]. And in particular, amorphous Raney Ni-P alloy catalyst exhibits a superior turnover rate than undoped Raney Ni for the hydrogenation of glucose to sorbitol [41]. Although catalysts that have been tuned by manipulating factors such as morphology, crystallinity and composition have been applied in various catalytic reactions, to the best of our knowledge, for biomass conversion, the influence of metal morphology coupled with crystallinity and composition effect on catalytic performance and product selectivity is rarely studied. In particular, there are no relevant studies for this specific parameter in glucose hydrogenation. Therefore, a fundamental study aiming at understanding structural factors in this reaction can potentially provide implications for the design of novel catalysts for biomass conversion.

Based on this, we prepared Ni nanospheres and Ni nanorods with different crystallinities and compositions by modulating the pressure of hydrogen during the synthesis. This differs from the usual strategies that imply controlling the concentration of the surfactants used as stabilizing agents [42]. Then, a third Ni nanostructured catalyst – namely nanobead chains was synthesized using a well-established method [43], and was applied to compare the catalytic performance with Ni nanospheres and nanorods in the glucose hydrogenation reaction. The comprehensive surface and bulk analysis of the three different Ni catalysts was carried out to clarify the reasons for their differences in catalytic performance and identify shape, crystallinity and composition factors that are unavoidably intimately entangled.

2. Materials and method

2.1. Chemicals and materials

Nickel(II) acetylacetonate ($Ni(acac)_2$) [$Ni(C_5H_7O_2)_2$, 95 %, Sigma-Aldrich], hexadecylamine (HDA) [$CH_3(CH_2)_{15}NH_2$, 90 %, Sigma-Aldrich], Nickel chloride hexahydrate [$NiCl_2$ $6H_2O$, 99.95 %, Alfa Aesar], trioctylphosphine (TOP) [$[CH_3(CH_2)_7]_3P$, 97 %, Sigma-Aldrich], mesitylene [$C_6H_3(CH_3)_3$, 98 %, Sigma-Aldrich], polyvinylpyrrolidone (PVP 40000) [$(CH_6H_9NO)_n$, Sigma-Aldrich], hydrazine hydrate [N_2H_4 H_2O, 99+%, Fisher Chemical], toluene [C_7H_8, 99.85 %, Acros Organics], ethylene glycol (EG) [$HOCH_2CH_2OH$, 99 %, Alfa Aesar], ethanol absolute [C_2H_5OH, 99.97 %, VWR Chemicals] and ethanol [C_2H_5OH, 99 %, VWR Chemicals] were used as received.

2.2. Catalysts preparation

2.2.1. Synthesis of Ni nanospheres and Ni nanorods catalysts

Synthesis of Ni nanospheres. The reagents used and their relative proportions were referred from the literature [44], but the synthesis conditions and purification steps were designed here. Briefly, 676.9 mg (2.5 mmol) of Ni $(acac)_2$ and 6.69 g (25 mmol) of HDA were dissolved in 42 mL of mesitylene in a 100 mL beaker with an oval stir bar (35 × 16 mm) introduced in advance. After a uniform solution was obtained, 0.62 mL (1.25 mmol) of TOP was added. Then the beaker was immediately placed inside a 300 mL stainless-steel high-pressure reactor. The reactor was degassed under vacuum and put under hydrogen 5 times, and finally filled with hydrogen at a pressure of 2 bar at room temperature. Then the reactor was heated until 180 °C with a heating rate of 5 °C per minute and left to react for 19 h with a stirring speed of 400 rpm. After 19 h, the beaker was taken out of the reactor at a temperature around 50 °C. All the formed particles were attached to the magnetic stirring bar. The particles were transferred from the stirring bar into a clean beaker for further purification, as described below.

Synthesis of Ni nanorods. The same reactants were used as for the nanospheres but different experimental conditions and set-ups were used: namely 676.9 mg (2.5 mmol) of Ni $(acac)_2$ and 6.69 g (25 mmol) of HDA were dissolved in 42 mL of mesitylene in a 100 mL one-neck round-bottom flask, and an oval stir bar (35 × 16 mm) was introduced in advance. After the flask was degassed and refilled with Argon for 3 times, it was subjected to ultrasounds for 30 min. 0.62 mL (1.25 mmol) of TOP was injected into the flask, then the flask was degassed under vacuum and filled with hydrogen 5 times and kept under hydrogen atmosphere with two individual balloons. Then the flask was heated until 180 °C with a heating rate of 5 °C per minute and left to react for 19 h with a stirring speed of 375 rpm. This stirring speed was adjusted to maintain similar mixing conditions than in the synthesis of the nanospheres described above. After 19 h, all the particles were attached to the magnetic stirring bar. Then the nanoparticles were transferred from the stirring bar into a clean beaker for further purification, as described below.

Synthesis of Ni nanobead chains. The preparation method followed Wen's work.[43] Briefly, 3 g of PVP-40000 was dissolved in 150 mL of EG in a 250 mL round-bottom flask, then 0.75 mL of 1 M aqueous $NiCl_2$ solution was introduced with vigorous stirring using an oval magnetic stirring bar (35 × 16 mm). After the whole mixture was heated to 150 °C, 5 mL of N_2H_4 H_2O was added, dropwise with a stirring speed of 500 rpm. The mixture was maintained at this temperature for 12 min. Then a dark grey product was formed. The product was separated by a strong magnet and transferred into a clean beaker for further purification, as described below.

Products purification: For Ni nanospheres and nanorods, the separated products were dispersed into 30 mL of toluene. After 2 min ultrasonication, the particles were separated by a magnet. Then 30 mL of a mixture of toluene and ethanol (1:1) was added to the particles and they were redispersed into the solution using ultrasounds. The particles were again separated by a magnet and the liquid was decanted leaving only the particles. This process was repeated 6 times, then the product was dried in a vacuum oven at room temperature overnight.

For Ni nanobead chains, the product was dispersed into 30 mL of deionized (DI) water by ultrasonication and separated by magnetic decantation, repeating this 3 times. Then it was washed with ethanol an-

other 3 times using the same procedure. After the product was further washed with absolute ethanol, it was dried in a vacuum oven at room temperature overnight. Finally, the catalysts were collected, grinded with an agate mortar and pestle, and stored in screw thread vials without any further treatments. In a typical synthesis, 90–98 mg of Ni nanospheres/rods were obtained, which corresponds to a yield of 61–67 %. For nanobead chains, 42–45 mg of Ni particles were obtained, corresponding to 90–96 % yield.

2.3. Characterization methods

Transmission electron microscopy (TEM) and high resolution TEM (HR-TEM) were performed by using JEOL 2100 LaB6 with a 0.2 nm point to point resolution. Dark field images were recorded after selecting parts of diffraction rings in order to observe the corresponding lighted area, i.e. oriented crystals.

SEM images were obtained on a field-emission scanning electron microscope JEOL 7600F operating at 15 kV. A small amount of sample was collected with a spatula and deposited on a carbon double-sided sticker bonded on a 26 mm diameter specimen holder, then air spray was used to remove the excess particles.

The attenuated total reflection (ATR) infrared spectroscopy spectra were recorded on a PerkinElmer Spectrum two instrument in the rage of 500–4000 cm^{-1} at room temperature. A small amount of sample was placed over the surface of the diamond crystal in the centre of the circular mounting plate in the instrument.

Raman spectra at room temperature were recorded using Thermo Scientific DXR Raman Microscope in the backscatting configuration with a 532 nm green laser. A small amount of sample was placed in the centre of a microslide, then another slide was gently pressed once on top of the sample and removed. Then, the slide with sample was placed on the worktable of the Microscope. The accumulation time and spot size of the laser used were 120 s and 865 nm, respectively, and a 50× objective was used on an Olympus microscope.

X-ray photoelectron spectroscopy (XPS) analyses were carried out at room temperature with an SSI-X-probe (SSX 100/206) photoelectron spectrometer from Surface Science Instruments (USA), equipped with a monochromatized microfocus Al X-ray source (1486.6 eV). Samples were set on the sample holders by double face adhesive tape. Charging effect of the samples were eliminated by placing a nickel grid above the samples and using a flood gun set at 8 eV. The pass energy was set at 150 eV. All the binding energies were calculated according to the C-(C, H) component of the C 1 s peak fixed at 284.8 eV. Data analysis was carried out using CasaXPS software, and the peaks were decomposed by Gaussian/Lorentzian product formula GL(15) after a Shirley-type background was subtracted.

Elemental analysis was carried out using ICP-AES Varian 720ES by analytical and chemical consultancy services from MEDAC ltd (UK). The samples were digested with 5 mL of nitric acid and 1 mL of hydrogen peroxide, then the solutions were made up to a volume with 18.2 Mohm water and analysed.

X-ray diffraction (XRD) experiments were performed using a Bruker D8 advanced diffractometer equipped with a Linkeye XE-T detector and operating at 40 kV and 30 mA. X-ray diffractograms were recorded from 30 to 80° (2θ) using an increment of 0.015° and an integration time of 0.15 s. EVA software (Bruker) was used for data analysis and the PDF-2 (2004) database was used for phase identification. Crystallinities of the samples were computed using the 'Crystallinity' function in DIFFRAC.EVA software, and the formulas used to compute the amorphousness and crystallinity percentage are as follows:

$$\%\text{Amorphous} = \frac{Globalarea - Reducedarea}{Globalarea} \times 100$$

$$\%\text{Crystallinity} = 100 - \%\text{Amorphous}$$

Global area: background with a 0.01 curvature taken automatically. Reduced area: background adjusted. For the background adjustment, the curvature and threshold are both set at the default value (1). The scan range from 37.7 to 48.2° was chosen to compute the crystallinity and the enhanced method was used to draw a smooth background with the assumption that there is only one single 'hump', which refers to diffraction peak Ni (1 1 1).

The specific surface area of the catalysts was measured through nitrogen adsorption–desorption isotherms, which was performed in a Micromeritics ASAP 2020 analyser at 77 K. Before analysis, the samples (around 0.2 g) were degassed for 2 h at 473 K with a heating rate of 10 K/min under 0.133 Pa pressure. The specific surface areas were calculated based on the Brunauer-Emmett-Teller (BET) equation by analysis of the isotherms.

For all the characterizations, as-prepared samples were used without any specific pre-treatment.

2.4. Hydrogenation of D-glucose

Hydrogenation experiments were performed in a stainless-steel high-pressure reactor (Parr autoclave). 12 mg of catalyst was added to the aqueous glucose solution of 100 mL with a concentration of 5 g/L, then the reactor was purged with N_2 for 5 min to remove air. The reaction mixture was subsequently heated to the set temperature (within the range 140–160 °C) under N_2, then the autoclave was filled to a constant H_2 pressure (30 bar) and the reaction started after turning on the stirring with a speed of 1700 rpm (which was sufficient to eliminate external mass-transport limitations). Samples were periodically withdrawn from the reaction vessel and filtrated on PVDF membrane (0.2 μm) to evaluate the evolution with time of both glucose conversion and products yields using HPLC. HPLC analysis was performed on filtrates with a Waters system equipped with a refractive index 2414 detector. An HPX-87C carbohydrate column was used, with ultrapure water as mobile phase at a flow rate of 0.5 $cm^3\ min^{-1}$, a column temperature of 358 K and 25 μl of injected volume. Standard alpha-D (+)-glucose ($C_6H_{12}O_6$, ≥99 %, Acros), D-(-)-fructose ($C_6H_{12}O_6$, ≥99 %, Sigma), D-(+)-mannose ($C_6H_{12}O_6$, ≥99 %, Sigma), D-mannitol ($C_6H_{14}O_6$, ≥98 %, Sigma-aldrich) and D-sorbitol ($C_6H_{14}O_6$, ≥99.5 %, Sigma) were first analysed by HPLC to determine their retention times separately, which were used as references to identify the products of glucose hydrogenation. The glucose conversion, sorbitol selectivity, product percentage yield, sorbitol productivity and carbon balance were calculated according to equations 1–5:

$$Conversion\,(\%) = \frac{molesofglucose\,(t=0) - molesofglucose\,(t=i)}{molesofglucose\,(t=0)} \times 100 \quad (1)$$

$$Selectivity(\%) = \frac{molesofsorbitol(t=i)}{molesofglucose(t=0) - molesofglucose(t=i)} \times 100 \quad (2)$$

$$\text{Yield}\,(\backslash\ \%) = \frac{\text{moles of product (t = i)}}{\text{moles of glucose (t = 0)}} \times 100 \quad (3)$$

$$Sorbitolproductivity = \frac{mass_{sorbitol}}{time * mass_{catalyst}} \quad (4)$$

$$C_b\,(\%) = \frac{n_{glucose(t=i)} + n_{fructose} + n_{mannose} + n_{mannitol} + n_{sorbitol}}{n_{glucose(t=0)}} \times 100 \quad (5)$$

Leaching percentage of Ni were calculated by the equation below.

$$\text{Ni leaching percentage} = \frac{C_{leached} \times V_{solution}}{m_{initial}} \times 100 \quad (6)$$

$C_{leached}$ was the concentration of leached Ni species detected by Perkin Elmer 3100 Atomic Absorption Spectrometer (AAS) in reaction

filtrates, $V_{solution}$ represents the volume of reaction medium, and $m_{initial}$ was the total weight of Ni in the fresh catalyst engaged in the catalytic test.

3. Results and discussion

3.1. Catalysts preparation

Ni nanospheres and nanorods were obtained using the same reactants but different reaction conditions, mainly varying hydrogen pressure. The long chain amine HDA has been proven a suitable capping agent for nanocrystal synthesis, and TOP was reported as a stabilizing ligand in the formation and stabilization of Ni nanoparticles [45,46]. $Ni(acac)_2$ was used as a precursor, HAD and TOP were chosen to adsorb on specific crystal faces tuning the facial growth rates hence the shapes. Here, hydrogen pressure is a tuneable factor to affect the kinetic of Ni particle growth, resulting in the production of particles with different morphologies and structures. Under the condition of 2 bars hydrogen pressure, ordered arrays of single dispersed nanospheres were acquired, while Ni nanorod particles were obtained when the hydrogen pressure was about 1 bar. Thus, two different shapes of Ni nanoparticles were successfully achieved through altering the hydrogen pressure. In addition to hydrogen pressure, it is also significant to emphasize that temperature is a crucial factor to obtain Ni nanoparticles. Several temperatures have been attempted for the preparation of Ni nanoparticles (Table S1) and it was found that with a reaction temperature below 180 °C, magnetic Ni nanoparticles could not be obtained even when prolonging the reaction time until 46.5 h at 140 °C. For all failed cases, no particles appeared at the end of the reaction, leaving the reaction medium beige or black in colour, indicating the precursor was not well reduced. Thus, 180 °C is necessary for the preparation of both Ni nanosphere and nanorod nanoparticles. At this temperature, after 19 h' reaction, the reaction medium turned transparent or grey transparent without bluish colour, which was therefore set as the synthesis duration. Ni nanobead chain particles were directly prepared following the reported procedure without any modification.

3.2. Morphology, surface chemistry and composition of the catalysts

The morphology of different shapes of Ni particles was determined by the comprehensive analysis of SEM and TEM images (Fig. 1). As shown in Fig. 1a and b, regular Ni nanospheres were neatly self-assembled, forming three-dimensional stacks. The measured particle size differed in SEM and TEM due to different calibration of magnification and contrast.[47] Due to the TEM images displaying a clearer edge than SEM images, the particle size was measured on the TEM image in Fig. 1c, which gave 24.1 ± 0.8 nm with each particle being surrounded with a thin shell, while TEM micrographs show relatively homogeneous structures for nanobead chains and nanorods. Nanorods as shown in Fig. 1 d and e were organized in a random dispersion, with a 72.3 ± 3.5 nm in length and 15.5 ± 1 nm in width dimension also measured on the TEM image. Nanobead chains do not have a uniform length, but it is greater than 1.5 μm, seeing Fig. 1g - h, and are formed by stringing together nanospheres with a diameter of 98.3 ± 9.3 nm. This is consistent with results of the reference.[43] The measured particle sizes differed in SEM and TEM maybe due to combination of incon-

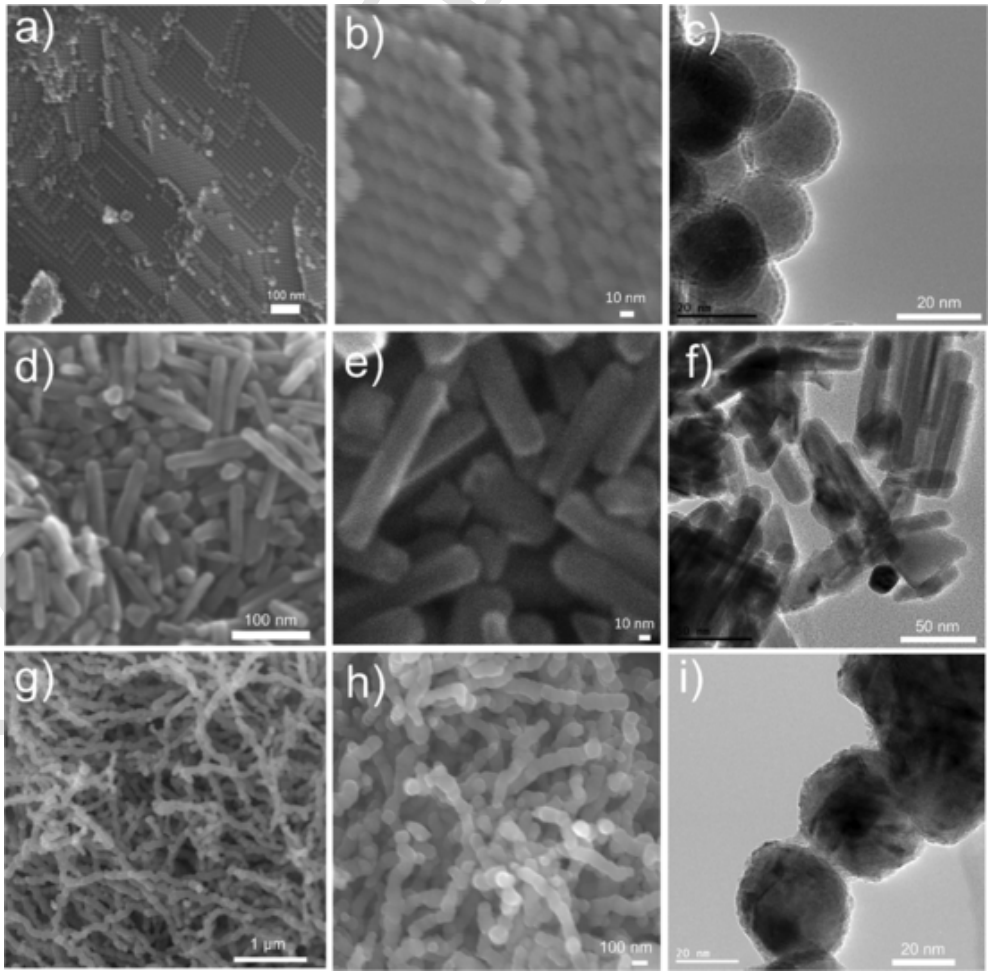

Fig. 1. SEM (left and center) and TEM (right column) images of Ni nanospheres (a–c), Ni nanorods (d–f) and nanobead chains (g–i).

sistent calibration of magnification and contrast.[47] TEM shows that nanospheres are connected to build anisotropic assemblies probably triggered by dipolar interactions. However, considering the polycrystalline beads, such an anisotropic shape cannot result from oriented crystal growth.

During the syntheses, large quantities of HDA and TOP were used as stabilizers for Ni nanospheres and nanorods, and surfactant PVP was applied for the preparation of Ni nanobead chains. Even after extensive washings during purification, those reagents could finally stay on the surface of the particles as surface agents, which would affect the catalytic performance by changing the surface chemical environment.[48] ATR-FTIR, Raman, and XPS were systematically applied to analyse the cleanliness of the surface of the catalysts.

Fig. 2a shows the ATR-FTIR spectra of prepared catalysts. All the spectra baselines slope down to the right, since all of the three samples in ash black colour display adsorption over the entire region from 4000 to 500 cm^{-1} and at low wavenumber this effect grows greater with deeper light penetration.[49] Those "spiky" peaks in the 3800 cm^{-1} region correspond to the active hydrogen bond of the O—H stretching vibration and bending mode of H_2O molecules in the atmosphere. The peak observed at 2349 cm^{-1} was assigned to O═C═O stretching of environmental CO_2. The broad peak around 1313 cm^{-1} in nanosphere sample may correspond to the C—N stretching and a slight sharp peak around 666 cm^{-1} existing in all three samples was ascribed to the N—H wagging mode of amine groups.[50] Both C—P stretching peaks of TOP at 1159, 1070 and 1023 cm^{-1} and N—H stretching and C—H stretching of HDA at 3330 cm^{-1} and 2916 cm^{-1} are absent in the spectra.[51] Moreover, no other vibration peaks appearing in the group frequency and fingerprint region of the three samples suggests that most stabilizing agents were washed away from the products. Similarly, the polarizability of the electrons in those organic molecules were not observed in Raman spectra, for instance, the longitudinal acoustical mode of primary amines around 144 cm^{-1} that would arise from HDA was absent [52] (Fig. 2b). Nevertheless, phonons within the Brillouin zone are active in Raman spectra. For Ni nanospheres, the approximately flat curve is due to the size of nanospheres being smaller than 30 nm and the loss in long range order.[53] The conservation of phonon momentum $\vec{q}$ in the oxidation layer of the Ni nanobead chains leaves as Raman active mode the zone centre ($q = 0$) optical phonon at 1058.3 cm^{-1}, 688.9 cm^{-1}, 517.3 cm^{-1} and 371.7 cm^{-1}, which correspond to $2P_{LO}$, $2P_{TO}$, $1P_{TO}$, $1P_{LO}$ of NiO vibrational modes, respectively.[54] Those phonon frequencies can also be observed in the Ni nanorod sample, but the observation of the narrow or broad humps differentiates between the nanorods and nanobead chain, and can be attributed to different long-range ordered structures within those two.[55,56] The steeply rising outline below 300 cm^{-1} is the elastically scattered laser radiation.[54].

In addition to IR and Raman acquisitions, XPS was also applied to assess the occurrence of the different elements at the surface of the materials. The atomic % of those elements calculated based on each high-resolution spectra are shown in Table 1. N was detected in all three Ni nanoparticles samples, as seen in the N 1 s high resolution spectra shown in Fig. S1. Peaks at 399.7 eV are corresponding to the amine group in remaining HDA for nanospheres and nanorods and N in PVP for nanobead chains. An additional nitrogen peak observed at 397.9 eV in the nanobead chains sample is associated with electronic donator-acceptor interactions between the chemisorbed PVP and Ni surface.[57] Although the same amount of HDA was used for the preparation of nanospheres and nanorods, the remaining N contents on their surfaces are slightly different, with 1.5 at.% on nanospheres and 0.6 at.% on nanorods. More N content existed in the nanobead chains originating from the usage of PVP during the synthesis. P was detected in nanospheres sample with 1.1 at.% on the surface, which may contribute to different compositions of the external thin layer observed in TEM image. Fig. 3a shows photoelectron measurement of P 2p core level. The phosphorus core level contains two main components. The lower binding energy peak observed at 130 eV corresponds to elemental phosphorus (P^0), which consists of the characteristic doublet representing the P^0 $2p_{3/2}$ and P^0 $2p_{1/2}$ orbitals with peak positions of 129.9 eV and 130.8 eV respectively.[58] This elemental phosphorus existing in nanospheres catalyst indicates the possible existence of a Ni-P phase, which could be a component positioned at the surface of Ni nanospheres. The peak centred at 133 eV in the spectra represents a pentoxide component such as P_2O_5 (P^{5+}), which also contains two sub-peaks of $P^{\delta+}$ $2p_{3/2}$ at 133.0 eV and $P^{\delta+}$ $2p_{1/2}$ at 134.2 eV [59,60]. The phosphorous oxide could come from the surface oxidation when phosphorus was exposed to air [61]. Apart from N and P, more than 90 at. % of the elements on the surface were C and O, which may be derived from the remaining organic species, surface oxidation and surface contamination by adventitious carbon [44,62]. This could affect the chemical state of Ni on the surface. Thus, high resolution XPS of Ni were recorded to identify its chemical state. Those XPS spectra of Ni $2p_{3/2}$ for the three catalysts are shown in Fig. 3b and the calculated atomic percentage in oxidation and metal states are displayed in Table 1. The binding energies around 852 eV and 855 eV are assigned to metallic Ni (Ni^0) and oxidized Ni ($Ni^{\delta+}$), respectively, along with satellite peaks [63]. Since the catalysts were stored without particular precautions, an external Ni oxide layer could be formed due to the contact with air [44], which explains the presence of oxidized Ni. NiO, $Ni(OH)_2$ and NiOOH are most expected to be the components of this oxidized Ni. A 0.9 eV shift of oxidized Ni peak was observed in nanospheres sample, which could be due to the fact that the relative content of NiOOH is higher in this sample than in the other two samples. Also, the presence of P_2O_5 species in nanospheres also leads to this shift. Similar percentages of metallic Ni

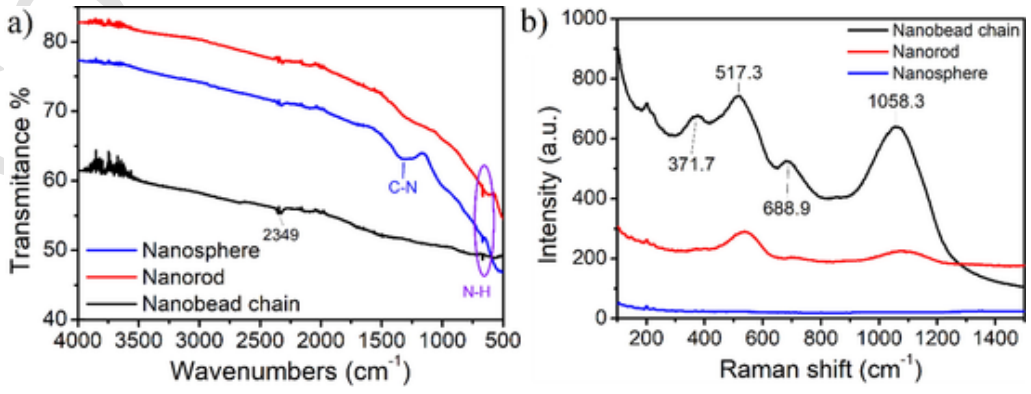

Fig. 2. ATR-FTIR spectra (a) and Raman spectra (b) of Ni nanospheres (blue), nanorods (red) and nanobead chains (black). (For interpretation of the references to colour in this figure legend, the reader is referred to the web version of this article.)

Table 1
Atomic percentages of C, N, Ni, O and P determined by XPS measurement; Binding energy and contents of Ni^0, $Ni^{\delta+}$ in Ni $2p_{3/2}$ level.

Ni particles	C 1s %	N 1s %	Ni 2p3 %	O 1s %	P 2p %	Ni^0 $2p_{3/2}$		$Ni^{\delta+}$ $2p_{3/2}$	
						B.E. (eV)	at.%	B.E. (eV)	at.%
Nanospheres	50.4	1.5	5.1	42.0	1.1	852.5	28.3	856	71.7
Nanorods	61.5	0.6	4.1	33.9	0.0	852.4	28.9	855.1	71.1
Nanobead chains	47.5	2.6	6.8	43.1	0.0	852.1	24.3	855.3	75.7

phase were detected on the near surface of nanosphere, nanorod, and nanobead chains catalysts.

Inductively coupled plasma optical emission spectrometry (ICP-OES) analyses were carried out to determine the elemental composition in the bulk material of the three Ni catalysts, and the results are shown in Table S2. N was detected in less than 0.1 wt% quantity in all three catalysts while 8.02 wt% of P was present in the bulk of nanosphere catalyst and none in the two others, which is consistent with results of XPS characterization. Since the content of P detected by ICP (*ca.* 9 at.%) is higher than by XPS (1.1 at.%), P dopant should distribute both in the external and internal volumes of the nanosphere particles.

Thus, most of the reactants were well removed from the surfaces of the catalysts after washing, but the adsorption of some species on the surface cannot be totally eliminated even with deliberate washing. Moreover, surface oxidation was found in the three Ni catalysts, and phosphorus as an impurity was only detected in Ni nanospheres catalysts. The possible phases identification within the three catalysts will be elaborated below.

3.3. Crystallinity of the catalysts

The power XRD patterns of three different catalysts are illustrated in Fig. 4. The diffraction peaks at $2\theta = 44.5^\circ$ in all samples corresponded to the (1 1 1) crystal planes of crystalline face centered cubic (fcc) nickel, and the peaks at 2θ values of 51.8° and 76.4° in the nanorod and nanobead chain samples were assigned to the (2 0 0) and (2 2 0) crystal planes of fcc nickel (JCPDS-ICDD card No.04-0850). The low intensity of the broad (1 1 1) diffraction peak in the nanospheres indicates small crystal grain size in this catalyst. Particle size calculated using the Debye–Scherrer formula based on the full-width at half-maximum (FWHM) of the (1 1 1) diffraction peak in nanospheres catalyst was only 3.4 nm, which is much lower than the value measured by TEM (24 nm), indicating the low crystallinity and/poly-crystalline nature of the Ni nanospheres. Besides, the diffraction of (2 0 0) and (2 2 0) planes were not distinguished in the nanosphere catalyst. On the contrary, all diffraction peaks can be observed in the nanorod and nanobead chain catalysts, indicating their higher crystallinity compared to nanospheres. Those crystallinities of catalysts were further computed using the 'Crystallinity' function in DIFFRAC.EVA software and the results are shown in Table S3. For the bulk catalysts, the lowest crystallinity is in the nanospheres, where 84 % of the structure is amorphous. The crystallinity of nanorods and nanobead chains is 62 % and 79 %, respectively.

HR-TEM images and SAED patterns of nanospheres, nanorods and nanobead chains catalysts are shown in Fig. 5. The HR-TEM images (Fig. 5a–c) of the three catalysts have clear lattice fringes with a spacing of about 0.2 nm corresponding to the Ni (1 1 1) face. The SAED patterns of all three samples (Fig. 5d–f) show concentric circles, which are due to polycrystallinity in the nanostructures. The nanorods (Fig. 5e) have a relatively more spotty pattern, while there are distinct diffused rings in the nanospheres and nanobead chains, which implies the existence of amorphous Ni, which implies an amorphous structure with short-range order but with defects. For the nanospheres (Fig. 5d), one clear and bright diffused ring was observed in the middle, which corresponds to Ni (1 1 1) plane. This Ni (1 1 1) diffraction ring is broader than that of nanorods and nanobead chains, which should be related to other amorphous phases associated with P.

Moreover, in order to disclose the amorphous structure of nanospheres catalyst during catalytic condition, an in situ p-XRD measurement was performed under reducing atmosphere mimicking the reducing condition of the hydrogenation reaction. In Fig. S2, it can be seen that before the sample was heated to 300 °C, there is only one hump around $2\theta = 44.5^\circ$, which is due to the diffraction contribution from fcc Ni (1 1 1) and amorphous structures, but once the temperature reached above 300 °C, more crystalline peaks appeared, implying a new phase formed. Those appeared new peaks, marked with '*', matched well with Ni_3P phase (JCPDS-ICDD card No.89-2743), regardless of the peaks shifts due to high temperature. All diffraction peaks from Ni_3P and Ni phases turned sharper and sharper with the increase of temperature, as expected. Thus, those amorphous Ni-P components can be confirmed to contribute to the broader Ni (1 1 1) diffraction ring observed with the nanospheres.

One question remains here about whether the introduction of hydrogen is involved in a reduction reaction that leads to the formation of the Ni_3P phase at high temperatures. Thus, nanospheres sample after heating up to 900 °C under N_2 atmosphere was analysis by p-XRD, separately. This result is shown in Fig. S3. It can be seen that under N_2 atmosphere, when the sample was heated to 900 °C, similarly, a new Ni_3P phase was formed and the Ni (1 1 1) is much sharper than its original hump. Thus, the temperature is the reason for the formation of the Ni_3P phase and the crystallization of Ni phase rather than a mere reduction reaction with hydrogen.

The diffraction rings of Ni (2 0 0) and Ni (2 2 0) in the nanospheres are not as clear as they are in nanorods and nanobead chains catalysts,

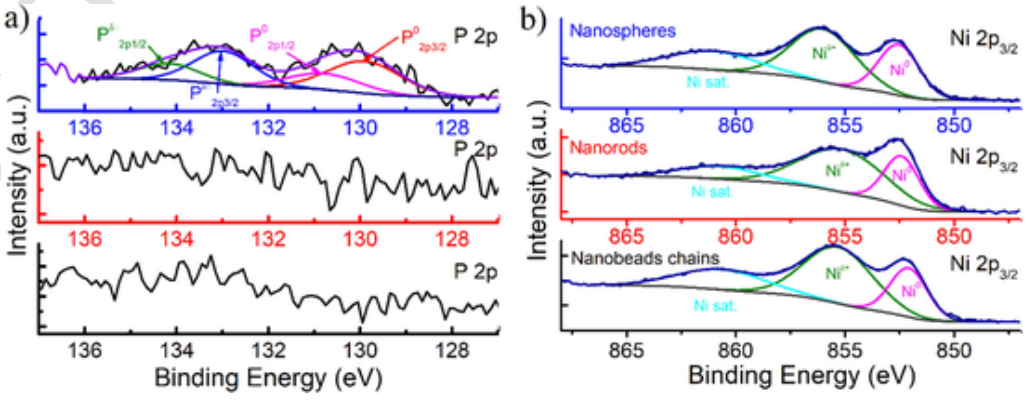

Fig. 3. High resolution P 2p (a) and Ni $2p_{3/2}$ (b) XPS spectra of nanospheres (blue), nanorods (red) and nanobeads chains (black). (For interpretation of the references to colour in this figure legend, the reader is referred to the web version of this article.)

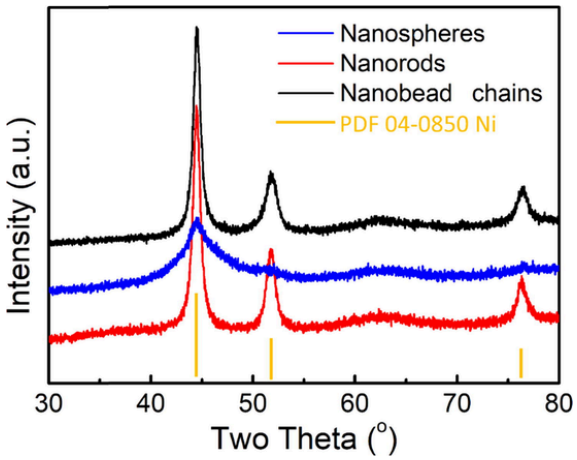

Fig. 4. XRD patterns of Ni nanospheres (blue), Ni nanorods (red) and Ni nanobead chains (black). (For interpretation of the references to colour in this figure legend, the reader is referred to the web version of this article.)

which is in complete agreement with the result of p-XRD. The crystallinity was also investigated by dark-field (DF) images. Fig. 6 illustrates DF images taken in different areas of the samples and at different angular beam tilts. The details of the corresponding bright-field images, SAED images and portions of diffraction ring chosen for DF imaging are illustrated in Figure S4-6.

In Fig. 6a–c, few bright spots with low contrast were observed in the nanospheres catalyst (circled in the images), suggesting low crystallinity for the nanospheres, while the lit up areas in the nanorod sample mostly stretched along the nanorods, forming short light lines rather than light spots as in nanospheres. In addition, the borders of the nanorods, corresponding to Ni (1 1 1) facets, were well illuminated (Fig. 6d–f). This is consistent with the clear presentation of boundary crystal planes on the edges of the nanoparticles as seen in Fig. 5b. The nanobead chains catalyst has more and larger bright spot areas than the nanospheres, but those lit up parts are also discrete (Fig. 6g–i). Thus, the nanorod catalyst presents a more continuous crystalline structure, especially in the outer layers of the particles, compared to the nanospheres and nanobead chains catalysts. This amorphous and low continuous crystalline structure of nanospheres can be further testified by the lowest magnetic moment of the nanospheres, as illustrated in Fig. S7. As it is shown in the picture, the three materials in glass vessels were placed in a same site under a permanent magnet. Nanorods and nanobead chains particles were drawn up by the magnet, but the nanospheres particles stayed at the bottom of the vessel.

The oxidized Ni phases on the surface of the three catalysts, detected by Raman and XPS, did not give a clear signal in XRD and SAED analyses. According to XRD patterns, it means that the oxide phase accounts for less than 5 wt%. Thus, Nickel samples were passivated rather than oxidized. Also, the diffraction peaks or patterns of Ni-P phase for nanospheres catalysts were not observed in XRD and SAED. This means that these oxidized Ni and Ni-P phases are in an amorphous state or have a low thickness of several angstroms to several nanometres maximum [44].

The reasons for particles with different components and crystallinities being obtained under different hydrogen pressures can be explained by the particle growth mechanism, involving nucleation and aggregation processes. The nucleation rate relates to the supersaturation of the solution – Lamer mechanism [64]. The $Ni^{(0)}$-TOP mononuclear complexes, such as $[Ni(TOP)_4]$ identified by Ely et al., should act as Ni-atom carriers, promoting the transmission of Ni [45,65]. Here, hydrogen as a reducing agent can elevate the formation rate of mononuclear complexes thanks to a higher concentration under a higher pressure [66]. Then, the kinetics of aggregation process is promoted with this higher concentration of mononuclear species, inducing that Ni atoms cannot be stabilized under thermodynamic condition. Thus, a hydrogen-undirected controlled aggregation of the nuclei leads to less crystallized particles under a higher pressure. And P is likely introduced into the particles as a dopant during this rapid aggregation process.

3.4. Physical adsorption properties of the catalysts

N_2 adsorption/desorption isotherms at −196 °C were measured to determine the specific surface area of those prepared catalysts. The isotherms and calculated BET surface areas are shown in Fig. S8. The expected Type II adsorption isotherm was obtained for all the samples, which indicates an indefinite multi-layer formation after completion of the monolayer adsorption. Type IV desorption isotherms were observed in nanosphere and nanorod samples, which corresponds to the

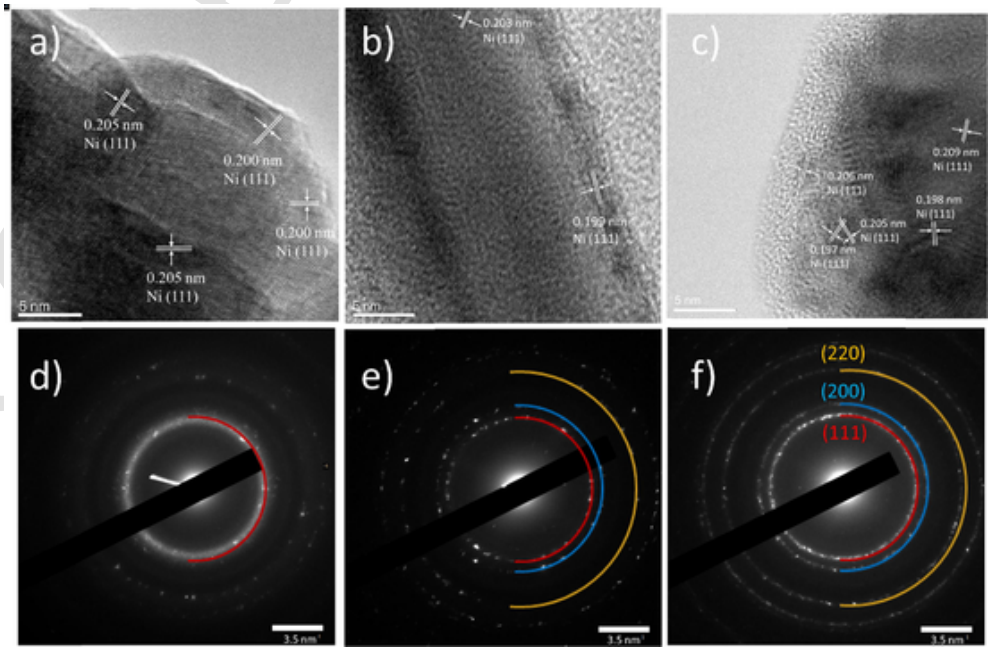

Fig. 5. HRTEM images and SAED patterns of Ni nanospheres (a, d), nanorods (b, e), nanobead chains catalysts (c, f).

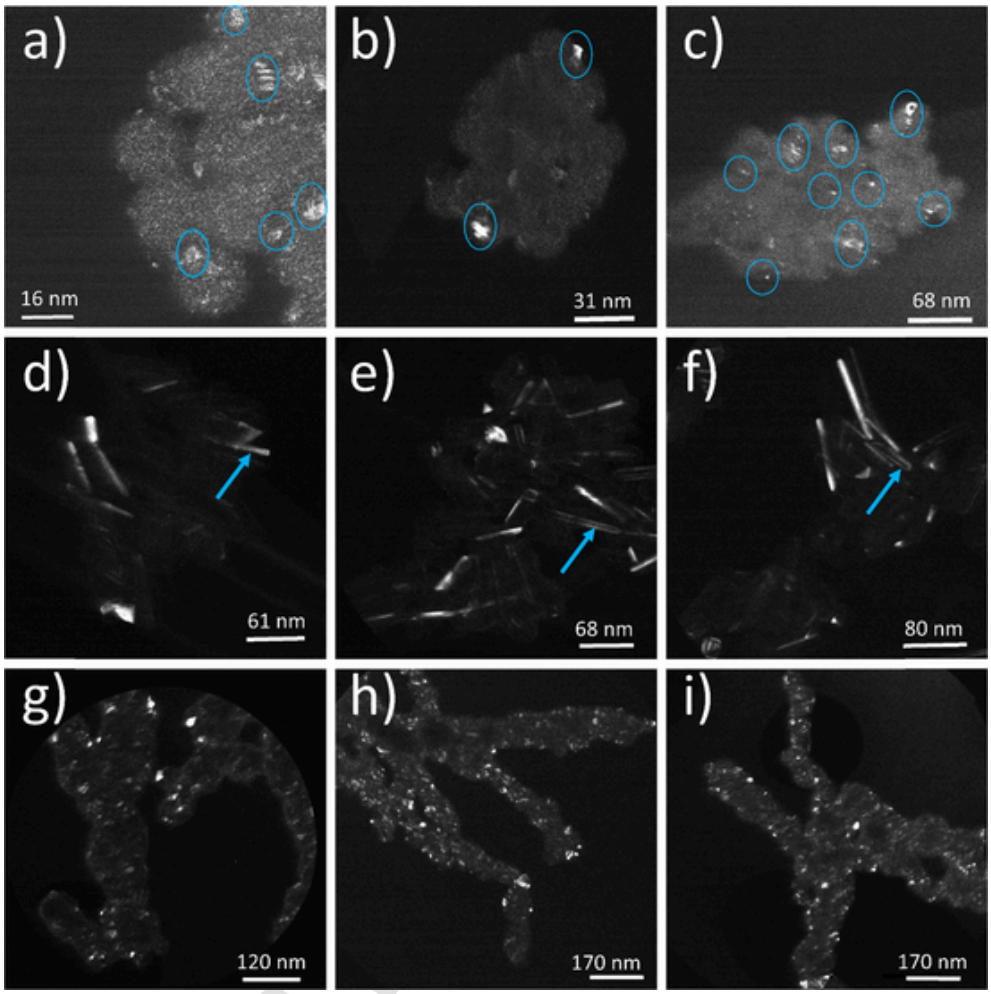

Fig. 6. Dark field images of nanospheres (a–c), nanorods (d–f), nanobead chains (g–i) catalysts.

presence of capillaries (mesopores) created by nanoparticles stacking. Since the length of nanobead chains are in the scale of μm, macropores are more likely formed during the particles stacking, which consequently gives a type II desorption isotherm in this case. The BET surface areas of nanospheres and nanorods are almost the same values (12 m^2/g), and higher than the surface area of the nanobead chains (6 m^2/g). The hysteresis loops in the isotherms of the nanospheres and nanorods indicated the slit holes in the samples formed by uniform particles accumulation (inter-grain voids). The hysteresis loop for nanospheres sample appears at lower relative pressure, which corresponds to the smaller slit pores in the nanospheres compared to nanorods. This is due to the fact that nanospheres are smaller in size than nanorods and therefore present smaller slit pores between the individual particles.

3.5. Catalytic performance of the catalysts in glucose hydrogenation reaction

After obtaining different shapes of Ni nanoparticles, we used them to catalyse the reaction of glucose hydrogenation. The catalytic cycle can be simply expressed as in Fig. 7a. Briefly, hydrogen chemisorbed on the catalyst surface, forms activated H adatoms. The substrate glucose adsorbs on the Ni surface either via O (1), O (5), and O (6) of glucopyranose or oxygen lone pair in the carbonyl group of glucose aldehydic

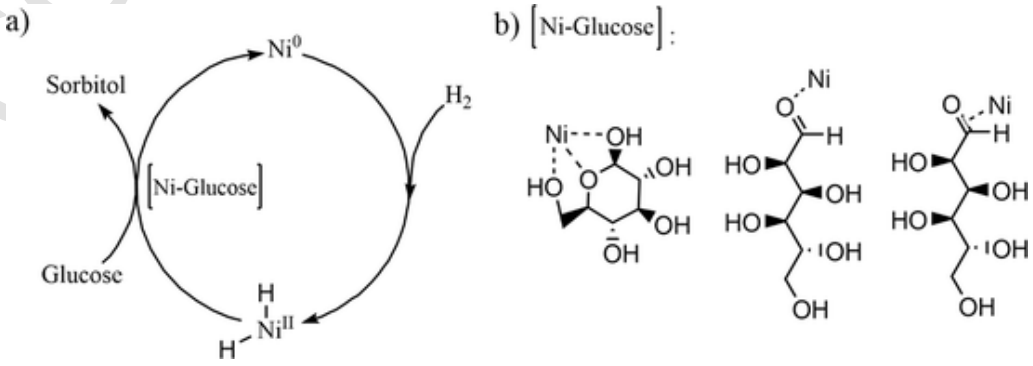

Fig. 7. (a) Catalytic cycle of glucose hydrogenation to sorbitol on Ni. (b) Adsorption structures of glucose on Ni [10,20,67].

form with η1(O) or η2 (C, O) configurations (Fig. 7b) [10,20,67]. The H adatoms can behave as nucleophiles and consequently do a substitution on the C (1) of glucopyranose or an addition onto the carbon atom of the polarized C═O bond of the glucose open-chain form. The resulting alkoxides are then protonated and finally sorbitol is produced after it desorbs from the metal surface.

Fig. 8 shows the evolution trend of glucose conversion with time over the three catalysts, including the results at different reaction temperatures. In order to eliminate any decrease in reaction rate due to mass transfer during the reaction, the conversion of the reaction was controlled below 30 %. It can be seen that the conversion of glucose increases with increased reaction temperature for the same reaction time, regardless of the type of catalysts used. The conversion of glucose over nanospheres catalysts was the highest at any temperature in the range from 140 to 160 °C, followed by nanobead chains and finally the nanorod catalysts. Turn over frequency (TOF) values should ideally be calculated here to compare the catalytic performance of the three catalysts, based on hydrogen chemisorption measurement to obtain the total number of active sites. The pre-treatment temperature to reduce the passivation layer on the catalysts should be kept below 300 °C to avoid sintering and new phase formation in the samples (as demonstrated by in situ XRD, see Fig. S2). However, this temperature is not enough, and very low hydrogen adsorptions were obtained after a pre-treatment at 250 °C. This results in a huge and unrealistic calculated TOF values. In reality, during the catalytic tests, the hydrogen pressure is much higher, resulting in Ni passivation layer reduction at much lower temperature. Thus, the sorbitol productivity at a same glucose conversion value was calculated instead of TOF, as shown in Table 2. It

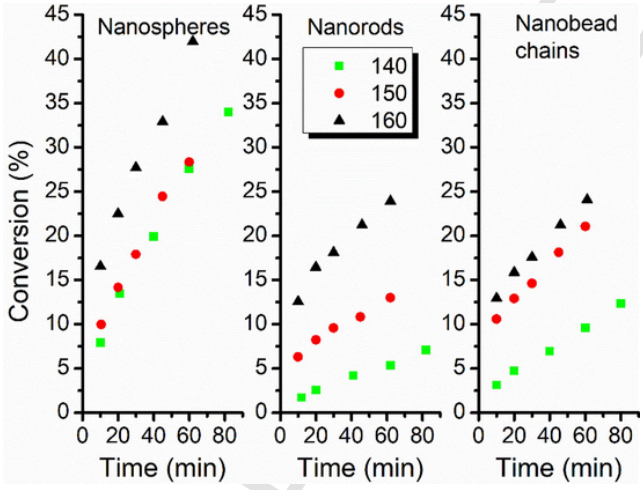

Fig. 8. Evolution of glucose conversion over time at 140 °C (green), 150 °C (red) and 160 °C (black) over nanospheres (left), nanorods (middle) and nanobead chains catalysts (right) under 30 bar of hydrogen. (For interpretation of the references to colour in this figure legend, the reader is referred to the web version of this article.)

can be seen that the nanospheres catalyst exhibited the highest value compared to the other two catalysts at all three temperatures.

The tendencies for the curves of glucose conversions vs time are consistent with the previously reported first-order reaction [68,69]. Therefore, the reaction rate constants for the glucose hydrogenation reaction at different reaction temperatures over different catalysts were obtained by plotting ln (1 − x) versus reaction time through a linear fit to the equation below(Eq. (7)), where × represents the glucose conversion and k represents reaction rate constant. The fitted curves are shown in Fig. S9. Furthermore, the apparent activation energies of the reaction over the three catalysts were obtained by graphing the natural logarithm of the Arrhenius equation (Eq. (8)), where A is the pre-exponential factor; E_a is the activation energy; R is the universal gas constant and T is the absolute temperature in Kelvins [70].

$$\ln(1-x) = -kt \tag{7}$$

$$\ln k = \ln A - \frac{E_a}{RT} \tag{8}$$

The apparent activation energies of glucose hydrogenation reactions over nanosphere, nanorod, and nanobead chains catalysts were calculated as 32 kJ/mol, 98 kJ/mol, and 98 kJ/mol, respectively (Fig. 9). Thus, the apparent activation energies calculated for the glucose hydrogenation reaction in the temperature range of 397–433 K with nanosphere catalysts is lower than for the other two catalysts nanostructures, which is in good agreement with that observed for highly performant Ru/HYZ catalysts (32.9 kJ/mol) [71], Pt/SBA-15 catalysts(47 kJ/mol) [16], supported Ni (67 kJ/mol) catalysts [22], and Raney nickel catalysts (6–44 kJ/mol) [72]. The apparent E_a calculated with nanorods and nanobead chains catalysts were the same, which should imply the same catalytic performance. However, for E_a calculation with Arrhenius equation, a temperature input error induced by fluctuation of real reaction temperature leads to a low R-Square, which is the case for nanobead chains with a R-Square less than 0.9, making the E_a less reliable. In addition, E_a is temperature-dependent, and although nanorods and nanobead chains catalysts were calculated to exhibit a same E_a in the temperature range of 397–433 K, their catalytic performances may be different at a specific temperature. This will be discussed in detail below.

In the glucose hydrogenation reaction, due to the high temperature of the aqueous solution, other side reactions usually occur, such as isomerization of glucose to fructose or mannose via an intramolecular hydride shift, and further formation of other by-products, like mannitol from the hydrogenation of those isomers, which was described in detail in our previous work [29]. Therefore, the sorbitol selectivity is also an important criterion to evaluate the catalyst performance. The trends of sorbitol selectivity with glucose conversion over the three catalysts at different temperatures are compared in Fig. 10. A selectivity increase with glucose conversion was observed in all cases except nanospheres and nanorods at 140 °C. Glucose isomerization to fructose or mannose more easily reach their equilibrium compared to glucose hydrogenation to sorbitol in the initial stage of the reaction. Thus, more sorbitol was produced with longer reaction time along with a relative constant pro-

Table 2
Sorbitol productivities under different reaction conditions.

Temperature/°C	Catalyst	Glucose conversion/%	Catalyst content/mg	Time/min	Sorbitol/mg	Productivity/kg.g_{cat}^{-1}.min^{-1}
140	Spheres	8	14	10	38.4	274.3
140	Rods	7	14	82	19.5	16.9
140	Bead chains	7	14	40	19.7	35.2
150	Spheres	14	14	20	45.7	163.22
150	Rods	13	14	62	24.6	28.32
150	Bead chains	13	14	20	21.6	77.12
160	Spheres	22	14	20	48.9	174.62
160	Rods	21	14	46	15.6	24.22
160	Bead chains	21	14	46	21.7	33.7

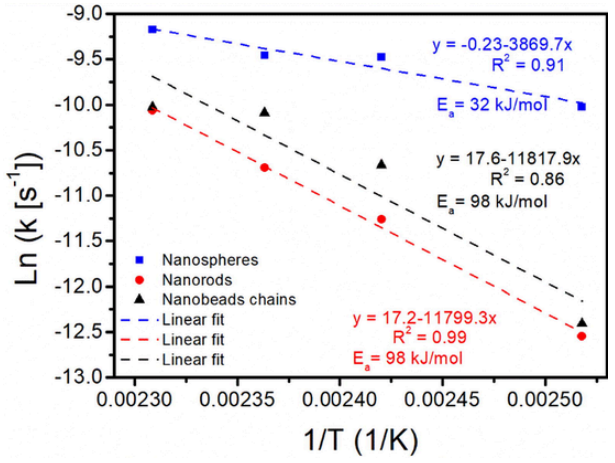

Fig. 9. Arrhenius plots for determination of the apparent activation energy E_a of glucose hydrogenation over nanospheres (blue), nanorods (red) and nanobead chains (black) from 397 to 443 K under 30 bar of hydrogen. (For interpretation of the references to colour in this figure legend, the reader is referred to the web version of this article.)

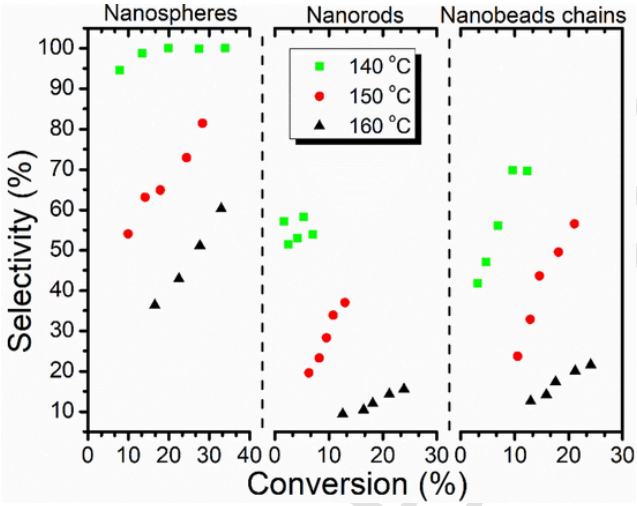

Fig. 10. Plots of sorbitol selectivity versus glucose conversion during glucose hydrogenation reaction over Ni nanospheres (left), Ni nanorods (middle), and Ni nanobead chains (right) at 140 °C (green), 150 °C (red) and 160 °C (black). (For interpretation of the references to colour in this figure legend, the reader is referred to the web version of this article.)

duction of fructose/mannose, which leads to the increased of selectivity of sorbitol with time. As side-reactions mentioned above are promoted along with the increase of temperature, consequently more fructose and mannitol are produced at higher temperature. Thus, higher sorbitol selectivity was obtained at lower reaction temperature in all three catalysts conditions. At a reaction temperature of 140 °C, the sorbitol selectivity remained essentially at 100 % for 1 h when using the nanospheres catalysts, while it was only about 55 % for the nanorods catalysts and 70 % for the nanobead chains catalysts. This 100 % sorbitol selectivity with nanospheres catalysts was also obtained in two repeated experiments (Table S4), which shows the repeatability of the catalytic performance. There is an increasing trend of the selectivity with glucose conversion at temperatures of 150 and 160 °C, which is due to the fact that the glucose isomerization reaction reaches an equilibrium at the beginning, producing a relatively stable amount of fructose. Regardless of the temperature conditions, the nanospheres catalyst exhibited the highest sorbitol selectivity, compared to the other nanorods and nanobead chains catalysts. The carbon balances (C_b) were calculated by Eq. (5). At the reaction temperature of 140 °C, all the C_b values were 100 % with the three catalysts over the whole time range. At 150 °C, there is only a 1 % difference of C_b values among the three catalysts with time and all those C_b are above 98 %. By opposition, all the C_b decreased from 100 % to around 91 % when the reactions were carried out at 160 °C (Fig. 11), and the remainder are unknown by-products possibly coming from glucose hydrolysis or dehydration reactions (see reaction scheme in Fig. S10). Nanospheres catalyst not only has highest catalytic activity, but also a definite advantage of highest sorbitol selectivity. A comparison of glucose conversion, sorbitol selectivity and TOFs with reported representative catalysts is shown in Table S5. Noble Ru-based catalysts have a prominent advantage in both activity and sorbitol selectivity. However, with monometallic Ni catalysts, it requires usually a longer reaction time and higher concentration of catalyst to reach a similar glucose conversion than with Ru-based catalysts, and this activity of Ni catalysts can be enhanced by promoters like B, Co, and Fe. Ni nanosphere catalysts in this work makes its activity even closer to Ru catalysts, because it achieved 34 % of glucose conversion and 100 % sorbitol selectivity in 82 min with only 0.0012 g of catalyst. The possible reasons for this outstanding catalytic performance observed with Ni nanospheres catalyst will be discussed now.

First, regarding the morphologies of nanospheres, nanorods and nanobead chains observed by SEM and TEM, surface crystalline facets distributions should vary among particles with different morphologies if they are monocrystalline [73–75]. However, polycrystalline structures were detected, especially on the surface of nanospheres and nanobead chains catalysts, which makes the surface facet enrichment indeterminable. While nanorods catalyst appear with a continuous crystalline structure - fcc Ni (1 1 1) in the external layers, it shows the lowest catalytic activity compared to nanosphere and nanobead chains catalysts, implying that the particles with polycrystalline nature on the surface are more active. In addition to the polycrystalline nature, amorphous Ni structures are coexisting in both nanosphere and nanobead chains catalysts. It has been studied that amorphous composition of the catalysts with abundant defects and coordination-unsaturated sites on the metal surface can potentially lead to higher catalytic performance than crystalline counterparts [76–78]. Therefore, the nanospheres with lowest crystallinity (highest content of amorphous nickel) has a better reactivity than the nanobead chains and nanorods.

It should be noted here that nanospheres, in addition to having the lowest crystallinity, also has a different component - P from the other two catalysts. Thus, in order to exclude the effect of P component, we tried to synthesize analogous P-free nanoparticles by changing the experimental conditions, but this was unsuccessful. In this case, P-free nanospheres with the same morphology cannot be obtained using the current synthesis method. However, comparisons can be made with the

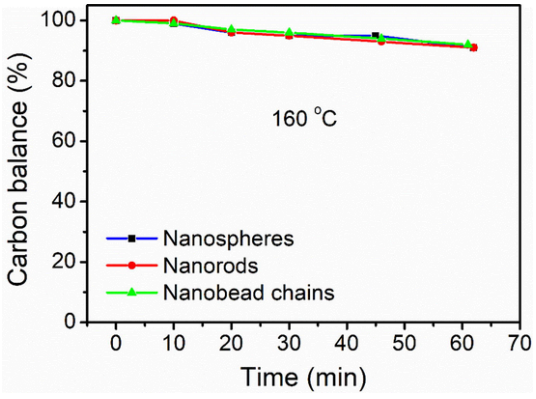

Fig. 11. Real-time carbon balance monitoring during glucose hydrogenation reaction over nanospheres (blue), nanorods (red) and nanobead chains (green) catalysts at 160 °C, 30 bar H_2, 1700 rpm and 62 min. (For interpretation of the references to colour in this figure legend, the reader is referred to the web version of this article.)

carbon black supported Ni nanoparticles CB-650 catalyst that we reported recently [79]. The Ni particles in CB-650 catalyst have a similar morphology to the Ni nanosphere catalyst described in this work - the average particle size is 24 nm and there is no P dopant, but Ni particles in CB-650 are carbon black (CB) supported. The specific characterization data of these catalysts are integrated in Table 3 below for a clearer comparison. It can be seen that under the same catalytic reaction conditions, comparing first the catalysts without P, the sorbitol productivity of CB-650 is lower than that of nanorods and nanobead chains catalysts. Both nanorods and nanobead chains have lower surface area and Ni^0 content than CB-650, which should give a lower sorbitol productivity, but the crystallinity of their nanoparticles is lower than that of CB-650, which confirms that lower crystallinity corresponds to higher catalyst activity. In addition, the sorbitol productivity obtained with P-free CB-650 (8 $kg{\cdot}g_{cat}^{-1}{\cdot}min^{-1}$) is even much lower than that of nanospheres with P component (274.3 $kg{\cdot}g_{cat}^{-1}{\cdot}min^{-1}$). Also, here, the low Ni^0 amount in the P-doped nanospheres does not make its sorbitol productivity lower than that of CB-650, because we believe that the passivation layer on Ni surface should be reduced in situ to form active sites since the hydrogenation reaction is carried out under 30 bar hydrogen.

Thus, it is the P component that decisively enhances the catalytic activity of nanospheres. As charge-transfer process is commonly occurring at the interface of a hybrid catalyst, this P dopant in the nanospheres catalysts can induce the electron transfer from Ni atom to P atom at the heterointerface of Ni-P phase, leading to positively charged Ni atoms, which has been demonstrated by density functional theory (DFT) calculations [80]. This can probably facilitate the glucose adsorption step with η1(O) or η2 (C, O) configurations. In addition, those positively charged Ni atoms can act as Lewis acid sites, resulting in an increase of the catalysts acidity. This may play a positive role for the formation of glucopyranose for a η1(O) configuration adsorption [81]. An hydrogen uptake rate was enhanced as well with P doping according to the reported Ni-P alloy catalyst study, from which the order of hydrogen uptake rate per gram Ni is Raney Ni-P > Raney Ni [41]. Furthermore, the doping P atoms can separate the surface Ni atoms and potentially create more amorphous structure, consequently more low-coordinated atoms. As Ni-P crystalline phase was not detected by Raman, SEAD pattern and p-XRD, but it started to be visible when nanospheres were heated at more than 300 °C, an intrinsic amorphous Ni-P structure is suggested. Therefore, P dopant in nanosphere catalyst has a contribution to its catalytic activity both in tuning the electron distribution among adjacent atoms and crystallinity of the material.

Besides, the organic capping agents not being detected by IR and Raman can be largely ignored for their effect on catalytic activity. The effect of surface chemical state of Ni could be excluded as well because the contents in metallic Ni on the surface of these three catalysts are similar. Moreover, similar specific surface areas and nonporous textures were measured for three catalysts, thus external and internal diffusion of the substrates during the reaction should show no difference among those three samples. Also, the difference in catalytic performance should not be due to a mere particle size effect, because the nanobead chains are much larger and thus display the lowest specific surface area than the nanorods in size, but have a higher catalytic activity than nanorods. Overall, amorphous structure and P dopant make Ni nanospheres an outstanding catalyst that outperforms Ni nanobead chains and nanorods.

3.6. Ni leaching from the three catalysts during catalytic reaction

Leaching of Ni in the three catalysts at three different temperatures after one-hour catalytic reaction was analysed by using AAS after filtering out the solid catalyst, and is in Table 4.

For all the Ni catalysts, after one hour reaction, 1.6–3 % of Ni leached at 140 °C; 1.4–2.7 % of Ni leached at 150 °C; and 1.6–5.7 % of Ni leached at 160 °C. Nanobead chains catalyst appears to leach less than either of the other two catalysts, which could be attributed to its high crystallinity. Similarly, the highest content of amorphous structure in nanospheres makes it leach the most at all temperatures. The identification of specific mechanisms of leaching and solutions to mitigate it are still under study, and are beyond the scope of the present contribution.

4. Conclusions

Three different morphologies of Ni nanoparticles, namely nanospheres, nanorods, nanobead chains, were successfully prepared for investigating comparatively their catalytic performance in the glucose hydrogenation reaction. By altering the hydrogen pressure during the synthesis, Ni nanospheres and Ni nanobead chains nanoparticles with different compositions and crystallinities were obtained, together with a temperature of 180 °C which was demonstrated to be a necessary condition for forming magnetic Ni nanoparticles. Magnetism was taken as a criteria to identify formation of metallic Ni nanoparticles. Decent washing steps were applied to remove the reactants after the synthesis, and as a consequence, HDA and TOP were not detected in the IR and Raman spectra of the final particles. NiO phase was probed by Raman spectra for Ni nanorods and Ni nanobead chains, but it was invisible in XRD pattern and SAED images, attributed to its amorphous structure and thin layers with less than 5 wt% contents. XPS and ICP test indicated the presence of a Ni-P component in Ni nanospheres catalysts, and this component was again not observed by XRD and SAED, suggesting its amorphous structure. These differences in crystallinity and composition ultimately led to significant differences in the catalytic performance of the three catalysts. Thus, activation energies of 32 kJ/mol, 98 kJ/mol, and 98 kJ/mol were attained for the glucose hydrogenation reaction catalysed with Ni nanospheres, Ni nanorods and Ni nanobead chains catalysts, respectively. In addition to the best catalytic activity obtained with Ni nanospheres, the highest selectivity in sorbitol was also achieved with Ni nanospheres, which is around 100 % at a typical reaction temperature of 140 °C. Thus, amorphous P-doped Ni nanospheres has not only superior catalytic activity but also excellent product selectivity contrasting with Ni nanorods and nanobead chains. Besides, the Ni leaching after catalytic reaction was also investigated, and it was found that the leaching percentage of Ni could be related to the crystallinity of the particles, that is, nanosphere owning the highest proportion of amorphous structure leached the most. Here, multiple factors working together led to building a high-performance catalyst, and this makes a meaningful contribution to P doped catalysts family with

Table 3
Structural properties and sorbitol productivity comparisons among nanosphere, nanorods, nanobead chains and CB-650 catalysts.

	Particle size/nm	P content/%	Surface Ni^0 content/%	Crystallinity/%	BET specific surface area/$m^2\ g^{-1}$	Productivity/$kg{\cdot}g_{cat}^{-1}{\cdot}min^{-1}$
Nanosphere	24.1 ± 0.8	8.02	28.3	16	12	274.3
Nanorods	72.3 ± 3.5 L * 15.5 ± 1 W	<0.01	28.9	62	12	16.9
Nanobead chains	>1.5 μm	<0.01	24.3	79	6	35.2
CB-650[#]	23.5 ± 11.6	0	84	100[*]	72	8

[#] Characterization data of CB-650 were extracted from our previous paper [79].
[*] Crystallinity was computed using the method mentioned in the Experimental part.

Table 4
Ni leaching percentage (%) from nanospheres, nanorods and nanobead chains catalysts after one-hour catalytic reaction at three reaction temperatures.

	140 °C	150 °C	160 °C
Nanospheres	3 ± 0.1	2.7 ± 0.1	5.7 ± 0.3
Nanorods	2.5 ± 0.1	1.8 ± 0.1	4 ± 0.3
Nanobead chains	1.6 ± 0.1	1.4 ± 0.1	1.6 ± 0.3

amorphous structure for the future design of green and efficient catalysts for similar types of reactions.

CRediT authorship contribution statement

Yang Fu : Methodology, Validation, Investigation, Writing – original draft, Visualization. **Benoit Pichon :** Investigation, Writing – review & editing. **François Devred :** Investigation, Writing – review & editing. **Michael L. Singleton :** Supervision, Writing – review & editing, Project administration. **Sophie Hermans :** Conceptualization, Methodology, Resources, Writing – review & editing, Supervision, Project administration, Funding acquisition.

Declaration of Competing Interest

The authors declare that they have no known competing financial interests or personal relationships that could have appeared to influence the work reported in this paper.

Data availability

Data will be made available on request.

Acknowledgements

The authors gratefully acknowledge Jean-François Statsyns for technical assistance, Dris Ihiawakrim for HRTEM measurements, Sabine Bebelman and Prof. Xavier Gonze for assistance and useful discussions for Raman analyses, Pierre Eloy for helpful support for XPS analysis. Y. F. thanks the China Scholarship Council (CSC) for the financial support.

Appendix A. Supplementary material

Supplementary data to this article can be found online at https://doi.org/10.1016/j.jcat.2022.09.028.

References

[1] D.L. Klass, Biomass for Renewable Energy, Fuels, and Chemicals, Elsevier, 1998.
[2] G.W. Huber, S. Iborra, A. Corma, Synthesis of transportation fuels from biomass: chemistry, catalysts, and engineering, Chem. Rev. 106 (2006) 4044–4098.
[3] L.-T. Fan, M.M. Gharpuray, Y.-H. Lee, Cellulose Hydrolysis, Springer Science & Business Media, 2012.
[4] P.L. Dhepe, M. Ohashi, S. Inagaki, M. Ichikawa, A. Fukuoka, Hydrolysis of sugars catalyzed by water-tolerant sulfonated mesoporous silicas, Catal. Lett. 102 (2005) 163–169.
[5] T. Werpy, G. Petersen, Top value added chemicals from biomass: volume I--results of screening for potential candidates from sugars and synthesis gas, National Renewable Energy Lab., Golden, CO (US), 2004.
[6] A. Fukuoka, P.L. Dhepe, Catalytic conversion of cellulose into sugar alcohols, Angew. Chem., Int. Ed. 45 (2006) 5161–5163.
[7] V.J. Ipatieff, Ber. dtsh. chem. Ges. (1912) 3218.
[8] P.J. Cerino, G. Fleche, P. Gallezot, J.P. Salome, Activity and stability of promoted Raney-Nickel catalysts in glucose hydrogenation, Stud. Surf. Sci. Catal. (1991) 231–236.
[9] W. Plazinski, A. Plazinska, M. Drach, The water-catalyzed mechanism of the ring-opening reaction of glucose, Phys. Chem. Chem. Phys. 17 (2015) 21622–21629.
[10] Q.T. Trinh, B.K. Chethana, S.H. Mushrif, Adsorption and reactivity of cellulosic aldoses on transition metals, J. Phys. Chem. C 119 (2015) 17137–17145.
[11] B. Hočevar, M. Grilc, M. Huš, B. Likozar, Mechanism, ab initio calculations and microkinetics of straight-chain alcohol, ether, ester, aldehyde and carboxylic acid hydrodeoxygenation over Ni-Mo catalyst, Chem. Eng. J. 359 (2019) 1339–1351.
[12] B. Hočevar, M. Grilc, M. Huš, B. Likozar, Mechanism, ab initio calculations and microkinetics of hydrogenation, hydrodeoxygenation, double bond migration and cis–trans isomerisation during hydrotreatment of C6 secondary alcohol species and ketones, Appl. Catal., B 218 (2017) 147–162.
[13] F.B. Bizhanov, R.B. Drozdova, Studies of the kinetics and mechanism of glucose hydrogenation over ruthenium catalysts, React. Kinet. Catal. Lett. 21 (1982) 35–39.
[14] F. Turek, R.K. Chakrabarti, R. Lange, R. Geike, W. Flock, On the experimental study and scale-up of three-phase catalytic reactors: Hydrogenation of glucose on nickel catalyst, Chem. Eng. Sci. 38 (1983) 275–283.
[15] E. Crezee, B.W. Hoffer, R.J. Berger, M. Makkee, F. Kapteijn, J.A. Moulijn, Three-phase hydrogenation of d-glucose over a carbon supported ruthenium catalyst—mass transfer and kinetics, Appl. Catal., A 251 (2003) 1–17.
[16] X. Zhang, L.J. Durndell, M.A. Isaacs, C.M.A. Parlett, A.F. Lee, K. Wilson, Platinum-catalyzed aqueous-phase hydrogenation of d-glucose to d-sorbitol, ACS Catal. 6 (2016) 7409–7417.
[17] A. Romero, A. Nieto-Márquez, E. Alonso, Bimetallic Ru:Ni/MCM-48 catalysts for the effective hydrogenation of D-glucose into sorbitol, Appl. Catal., A 529 (2017) 49–59.
[18] S. Esposito, B. Silvestri, V. Russo, B. Bonelli, M. Manzoli, F.A. Deorsola, A. Vergara, A. Aronne, M. Di Serio, Self-activating catalyst for glucose hydrogenation in the aqueous phase under mild conditions, ACS Catal. 9 (2019) 3426–3436.
[19] P. Gallezot, P.J. Cerino, B. Blanc, G. Flèche, P. Fuertes, Glucose hydrogenation on promoted raney-nickel catalysts, J. Catal. 146 (1994) 93–102.
[20] M. Makkee, A.P.G. Kieboom, H. van Bekkum, Hydrogenation of d-fructose and d-fructose/d-glucose mixtures, Carbohydr. Res. 138 (1985) 225–236.
[21] F.B. Bizhanov, D.V. Sokol'skii, N.I. Popov, N.Y. Malkhina, A.M. Khisametdinov, Kinet. Katal. 10 (1969) 655–660.
[22] B. Kusserow, S. Schimpf, P. Claus, Hydrogenation of glucose to sorbitol over nickel and ruthenium catalysts, Adv. Synth. Catal. 345 (2003) 289–299.
[23] X. Guo, X. Wang, J. Guan, X. Chen, Z. Qin, X. Mu, M. Xian, Selective hydrogenation of D-glucose to D-sorbitol over Ru/ZSM-5 catalysts, Cuihua Xuebao 35 (2014) 733–740.
[24] P.M. de Souza, L. Silvester, A.G.M. da Silva, C.G. Fernandes, T.S. Rodrigues, S. Paul, P.H.C. Camargo, R. Wojcieszak, Exploiting the synergetic behavior of PtPd bimetallic catalysts in the selective hydrogenation of glucose and furfural, Catalysts 9 (2019) 132.
[25] B.W. Hoffer, E. Crezee, P.R.M. Mooijman, A.D. Van Langeveld, F. Kapteijn, J.A. Moulijn, Carbon supported Ru catalysts as promising alternative for Raney-type Ni in the selective hydrogenation of D-glucose, Catal. Today 79–80 (2003) 35–41.
[26] H. Singh, A. Rai, R. Yadav, A.K. Sinha, Glucose hydrogenation to sorbitol over unsupported mesoporous Ni/NiO catalyst, Mol. Catal. 451 (2018) 186–191.
[27] B. Zada, L. Yan, Y. Fu, Effective conversion of cellobiose and glucose to sorbitol using non-noble bimetallic NiCo/HZSM-5 catalyst, Sci. China: Chem. 61 (2018) 1167–1174.
[28] S. Schimpf, C. Louis, P. Claus, Ni/SiO_2 catalysts prepared with ethylenediamine nickel precursors: influence of the pretreatment on the catalytic properties in glucose hydrogenation, Appl. Catal., A 318 (2007) 45–53.
[29] Y. Fu, L. Ding, M.L. Singleton, H. Idrissi, S. Hermans, Synergistic effects altering reaction pathways: the case of glucose hydrogenation over Fe-Ni catalysts, Appl. Catal., B 288 (2021) 119997.
[30] M.Y. Byun, D.-W. Park, M.S. Lee, Effect of sodium propionate as a stabilizer on the catalytic activity of Pt/C catalysts for d-glucose hydrogenation, Catal. Today 352 (2019) 88–94.
[31] H. Masatake, K. Tetsuhiko, S. Hiroshi, Y. Nobumasa, Novel gold catalysts for the oxidation of carbon monoxide at a temperature far below 0 °C, Chem. Lett. 16 (1987) 405–408.
[32] T.S. Ahmadi, Z.L. Wang, T.C. Green, A. Henglein, M.A. El-Sayed, Shape-controlled synthesis of colloidal platinum nanoparticles, Science 272 (1996) 1924–1925.
[33] B.R. Cuenya, Synthesis and catalytic properties of metal nanoparticles: size, shape, support, composition, and oxidation state effects, Thin Solid Films 518 (2010) 3127–3150.
[34] V. Komanicky, H. Iddir, K.-C. Chang, A. Menzel, G. Karapetrov, D. Hennessy, P. Zapol, H. You, Shape-dependent activity of platinum array catalyst, J. Am. Chem. Soc. 131 (2009) 5732–5733.
[35] M. Crespo-Quesada, S. Yoon, M. Jin, A. Prestianni, R. Cortese, F. Cárdenas-Lizana, D. Duca, A. Weidenkaff, L. Kiwi-Minsker, Shape-dependence of Pd nanocrystal carburization during acetylene hydrogenation, J. Phys. Chem. C 119 (2015) 1101–1107.
[36] R. Xu, D. Wang, J. Zhang, Y. Li, Shape-dependent catalytic activity of silver nanoparticles for the oxidation of styrene, Chem. Asian J. 1 (2006) 888–893.
[37] S.K. Kim, C. Kim, J.H. Lee, J. Kim, H. Lee, S.H. Moon, Performance of shape-controlled Pd nanoparticles in the selective hydrogenation of acetylene, J. Catal. 306 (2013) 146–154.
[38] J. Kibsgaard, C. Tsai, K. Chan, J.D. Benck, J.K. Nørskov, F. Abild-Pedersen, T.F. Jaramillo, Designing an improved transition metal phosphide catalyst for hydrogen evolution using experimental and theoretical trends, Energy Environ. Sci. 8 (2015) 3022–3029.
[39] B. Liu, N. Huang, Y. Wang, X. Lan, T. Wang, Promotion of inorganic phosphorus on Rh catalysts in styrene hydroformylation: geometric and electronic effects, ACS Catal. 11 (2021) 1787–1796.
[40] H. Li, W. Wang, H. Li, J.-F. Deng, Crystallization deactivation of Ni–P/SiO2 amorphous catalystand the stabilizing effect of silica support on the Ni–P amorphous structure, J. Catal. 194 (2000) 211–221.
[41] H. Li, W. Wang, J. Fa Deng, Glucose hydrogenation to sorbitol over a skeletal Ni-p amorphous alloy catalyst (Raney Ni-P), J. Catal. 191 (2000) 257–260.
[42] K. An, S. Alayoglu, T. Ewers, G.A. Somorjai, Colloid chemistry of nanocatalysts: a

molecular view, J. Colloid Interface Sci. 373 (2012) 1–13.
[43] Z. Xia, W. Wen, Synthesis of nickel nanowires with tunable characteristics, Nanomaterials 6 (2016) 19.
[44] A.P. LaGrow, B. Ingham, S. Cheong, G.V. Williams, C. Dotzler, M.F. Toney, D.A. Jefferson, E.C. Corbos, P.T. Bishop, J. Cookson, R.D. Tilley, Synthesis, alignment, and magnetic properties of monodisperse nickel nanocubes, J. Am. Chem. Soc. 134 (2012) 855–858.
[45] S. Carenco, C. Boissière, L. Nicole, C. Sanchez, P. Le Floch, N. Mézailles, Controlled design of size-tunable monodisperse nickel nanoparticles, Chem. Matter. 22 (2010) 1340–1349.
[46] S.L. Cumberland, K.M. Hanif, A. Javier, G.A. Khitrov, G.F. Strouse, S.M. Woessner, C.S. Yun, Inorganic clusters as single-source precursors for preparation of CdSe, ZnSe, and CdSe/ZnS nanomaterials, Chem. Mater. 14 (2002) 1576–1584.
[47] J. Tuoriniemi, A.-C.-J.-H. Johnsson, J.P. Holmberg, S. Gustafsson, J.A. Gallego-Urrea, E. Olsson, J.B.C. Pettersson, M. Hassellöv, Intermethod comparison of the particle size distributions of colloidal silica nanoparticles, Sci. Technol. Adv. Mater. 15 (2014) 035009.
[48] H. Lee, Utilization of shape-controlled nanoparticles as catalysts with enhanced activity and selectivity, RSC Adv. 4 (2014) 41017–41027.
[49] S.J. Parikh, K.W. Goyne, A.J. Margenot, F.N.D. Mukome, F.J. Calderón, Chapter one - soil chemical insights provided through vibrational spectroscopy, in: D.L. Sparks (Ed.), Advances in Agronomy, Academic Press, 2014, pp. 1–148.
[50] C. Mui, J.H. Han, G.T. Wang, C.B. Musgrave, S.F. Bent, Proton transfer reactions on semiconductor surfaces, J. Am. Chem. Soc. 124 (2002) 4027–4038.
[51] C.J. Pouchert, Aldrich Library of FT-IR Spectra, second ed., Aldrich, Milwaukee, WI, 1997.
[52] A.M.A. da Costa, C.F.G.C. Geraldes, J.J.C. Teixeira-Dias, A Raman spectroscopic study of molecular interaction in long-chain primary amines systems, J. Raman Spectrosc. 13 (1982) 56–62.
[53] I.H. Campbell, P.M. Fauchet, The effects of microcrystal size and shape on the one phonon Raman spectra of crystalline semiconductors, Solid State Commun. 58 (1986) 739–741.
[54] R.E. Dietz, G.I. Parisot, A.E. Meixner, Infrared absorption and raman scattering by two-magnon processes in NiO, Phys. Rev. B 4 (1971) 2302–2310.
[55] H. Richter, Z.P. Wang, L. Ley, The one phonon Raman spectrum in microcrystalline silicon, Solid State Commun. 39 (1981) 625–629.
[56] G. Gouadec, P. Colomban, Raman Spectroscopy of nanomaterials: How spectra relate to disorder, particle size and mechanical properties, Prog. Cryst. Growth Charact. Mater. 53 (2007) 1–56.
[57] L. Qiu, F. Liu, L. Zhao, W. Yang, J. Yao, Evidence of a unique electron donor–acceptor property for platinum nanoparticles as studied by XPS, Langmuir 22 (2006) 4480–4482.
[58] M. Shimizu, Y. Tsushima, S. Arai, Electrochemical na-insertion/extraction property of ni-coated black phosphorus prepared by an electroless deposition method, ACS Omega 2 (2017) 4306–4315.
[59] M.T. Edmonds, A. Tadich, A. Carvalho, A. Ziletti, K.M. O'Donnell, S.P. Koenig, D.F. Coker, B. Özyilmaz, A.H.C. Neto, M.S. Fuhrer, Creating a stable oxide at the surface of black phosphorus, ACS Appl. Mater. Interfaces 7 (2015) 14557–14562.
[60] W. Luo, D.Y. Zemlyanov, C.A. Milligan, Y. Du, L. Yang, Y. Wu, P.D. Ye, Surface chemistry of black phosphorus under a controlled oxidative environment, Nanotechnology 27 (2016) 434002.
[61] A. Ziletti, A. Carvalho, D.K. Campbell, D.F. Coker, A.H. Castro Neto, Oxygen defects in phosphorene, Phys. Rev. Lett. 114 (2015) 046801.
[62] A.W. Adamson, A.P. Gast, Physical Chemistry of Surfaces, sixth ed., Wiley, 1997.
[63] M.C. Biesinger, B.P. Payne, A.P. Grosvenor, L.W.M. Lau, A.R. Gerson, R.S.C. Smart, Resolving surface chemical states in XPS analysis of first row transition metals, oxides and hydroxides: Cr, Mn, Fe, Co and Ni, Appl. Surf. Sci. 257 (2011) 2717–2730.
[64] V.K. LaMer, R.H. Dinegar, Theory, production and mechanism of formation of monodispersed hydrosols, J. Am. Chem. Soc. 72 (1950) 4847–4854.
[65] T.O. Ely, C. Amiens, B. Chaudret, E. Snoeck, M. Verelst, M. Respaud, J.-M. Broto, Synthesis of nickel nanoparticles. influence of aggregation induced by modification of poly(vinylpyrrolidone) chain length on their magnetic properties, Chem. Matter. 11 (1999) 526–529.
[66] M.A. Watzky, R.G. Finke, Transition metal nanocluster formation kinetic and mechanistic studies. A new mechanism when hydrogen is the reductant: slow, continuous nucleation and fast autocatalytic surface growth, J. Am. Chem. Soc. 119 (1997) 10382–10400.
[67] P.J. Cerino, G. Fleche, P. Gallezot, J.P. Salome, Activity and stability of promoted raney-nickel catalysts in glucose hydrogenation, in: M. Guisnet, J. Barrault, C. Bouchoule, D. Duprez, G. Pérot, R. Maurel, C. Montassier (Eds.), Studies in Surface Science and Catalysis, Elsevier, 1991, pp. 231–236.
[68] M. Abdel Akher, J. Ghali, M.S. Raouf, M. Roushdi, Factors affecting the catalytic hydrogenation of D-glucose. Part I. Effect of type of catalyst and concentrations of both glucose and catalyst, Starch - Stärke 26 (1974) 307–312.
[69] J. Karolyi, Production of sorbitol by use of ammonia synthesis gas, Ind. Eng. Chem. Process Des. Dev. 7 (1968) 107–110.
[70] S. Arrhenius, Über die Dissociationswärme und den Einfluss der Temperatur auf den Dissociationsgrad der Elektrolyte, Z. Phys. Chem. 4U (1889) 96–116.
[71] D.K. Mishra, A.A. Dabbawala, J.J. Park, S.H. Jhung, J.-S. Hwang, Selective hydrogenation of d-glucose to d-sorbitol over HY zeolite supported ruthenium nanoparticles catalysts, Catal. Today 232 (2014) 99–107.
[72] B.W. Hoffer, E. Crezee, F. Devred, P.R.M. Mooijman, W.G. Sloof, P.J. Kooyman, A.D. Van Langeveld, F. Kapteijn, J.A. Moulijn, The role of the active phase of Raney-type Ni catalysts in the selective hydrogenation of D-glucose to D-sorbitol, Appl. Catal., A 253 (2003) 437–452.
[73] L. Vitos, A.V. Ruban, H.L. Skriver, J. Kollár, The surface energy of metals, Surf. Sci. 411 (1998) 186–202.
[74] G. Porwal, S. Gupta, S. Sreedhala, J. Elizabeth, T.S. Khan, M.A. Haider, C.P. Vinod, Mechanistic insights into the pathways of phenol hydrogenation on Pd nanostructures, ACS Sust. Chem. Eng. 7 (2019) 17126–17136.
[75] K. Murata, K. Ogura, J. Ohyama, K. Sawabe, Y. Yamamoto, S. Arai, A. Satsuma, Selective Hydrogenation of cinnamaldehyde over the stepped and plane surface of Pd nanoparticles with controlled morphologies by CO chemisorption, ACS Appl. Mater. Interf. 12 (2020) 26002–26012.
[76] H. Cheng, N. Yang, X. Liu, Q. Yun, M.H. Goh, B. Chen, X. Qi, Q. Lu, X. Chen, W. Liu, L. Gu, H. Zhang, Aging amorphous/crystalline heterophase PdCu nanosheets for catalytic reactions, Natl. Sci. Rev. 6 (2019) 955–961.
[77] R.D.L. Smith, M.S. Prévot, R.D. Fagan, Z. Zhang, P.A. Sedach, M.K.J. Siu, S. Trudel, C.P. Berlinguette, Photochemical route for accessing amorphous metal oxide materials for water oxidation catalysis, Science 340 (2013) 60–63.
[78] G. Wu, X. Zheng, P. Cui, H. Jiang, X. Wang, Y. Qu, W. Chen, Y. Lin, H. Li, X. Han, Y. Hu, P. Liu, Q. Zhang, J. Ge, Y. Yao, R. Sun, Y. Wu, L. Gu, X. Hong, Y. Li, A general synthesis approach for amorphous noble metal nanosheets, Nat. Commun. 10 (2019) 4855.
[79] Y. Fu, F. Devred, P. Eloy, T. Haynes, M.L. Singleton, S. Hermans, The effect of Ni particle size and carbon support on catalytic activity for glucose hydrogenation reaction, Appl. Catal. A 644 (2022) 118833.
[80] T. Liu, A. Li, C. Wang, W. Zhou, S. Liu, L. Guo, Interfacial electron transfer of Ni2P–NiP2 polymorphs inducing enhanced electrochemical properties, Adv. Mater. 30 (2018) 1803590.
[81] G. Gao, Y. Shao, Y. Gao, T. Wei, G. Gao, S. Zhang, Y. Wang, Q. Chen, X. Hu, Synergetic effects of hydrogenation and acidic sites in phosphorus-modified nickel catalysts for the selective conversion of furfural to cyclopentanone, Catal. Sci. Technol. 11 (2021) 575–593.